

Lattice Boltzmann simulations of the permeability and capillary adsorption of cement model microstructures

M. Zalzale^{*} and P. J. McDonald^{†,‡}

^{*} Laboratory of Construction Materials, Ecole Polytechnique Fédérale de Lausanne, CH-1015 Lausanne, Switzerland

[†] Department of Physics, University of Surrey, Guildford, Surrey, GU2 7XH, UK

[‡] Corresponding author, p.mcdonald@surrey.ac.uk

Abstract

The lattice Boltzmann method is used to investigate the permeability of microstructures of cement pastes generated using the numerical models CEMHYD3D (D.P. Bentz 1997) and μ IC (S. Bishnoi and K.L. Scrivener 2009). Results are reported as a function of paste water-to-cement ratio and degree of hydration. The permeability decreases with increasing hydration and decreasing water-to-cement ratio in agreement with experiment. However the permeability is larger than the experimental data recorded using beam bending methods (W. Vichit-Vadakan and G.W. Scherer 2002). Notwithstanding, the lattice Boltzmann results compare favourably with alternate numerical methods of permeability calculation for cement model microstructures. In addition, we show early results for the liquid / vapour capillary adsorption and desorption isotherms in the same model μ IC structures. The broad features of the experimental capillary porosity isotherm are reproduced, although further work is required to adequately parameterise the model.

Keywords

*Modeling (E), Transport Properties (C), Permeability (C), Adsorption (C), Lattice Boltzmann
(not included in the list).*

1. INTRODUCTION

Concrete is the most widely used construction material on Earth. It is estimated that production exceeds one cubic meter per person per year [1]. Although concrete is an inherently low CO₂ emission material per tonne compared to almost all other construction materials, this huge volume means that concrete production is responsible for between 5 and 8% of global CO₂ emissions [2]. The primary constituent of concrete is the binder: cement. Almost all of the emissions come from cement production: the breakdown of limestone to lime and CO₂. Reducing CO₂ emissions requires achieving two key objectives: the use of improved binders with greater fractions of supplementary cementitious materials; and the use of materials with improved, predictable, resistance to degradation for a longer life-cycle. At issue, is the fact that cement is a highly heterogeneous material for which the microstructure strongly affects performance. It comprises solid phases formed by chemical interaction of water and anhydrous cement with pore structures across a hierarchy of length scales. The pores range from sub-nanometre intra-sheet pores of the active component, calcium silicate hydrate (C-S-H), through gel pores on the 10 nm scale and on to micron scale capillary pores, cracks and voids. Water is found in all these environments and critically affects cement performance. During curing, water helps determine the evolution of the microstructure that leads to the development of mechanical properties. In cured material, water transport impacts strongly on durability both directly, e.g. freeze thaw action or indirectly by permitting the ingress of aggressive ions. Hence, understanding the link between pore-water interactions and transport in cement is crucial to understanding the link between microstructure and performance. Achieving this is a pre-requisite to achieving either of the primary objectives for new materials. Unfortunately, water is also a

major obstacle to progress since our understanding of pore-water interactions and transport in cement remains severely limited.

Two key experimental parameters related to water in cement are the permeability¹ and the water uptake as a function of relative humidity: the adsorption / desorption isotherm. They are at either end of a spectrum of properties that impact water transport.

The permeability characterises a porous medium from the perspective of saturated flow through it. Permeability therefore depends on the connectivity of the pore network and on the channel sizes. It is related to macroscopic observables through Darcy's law [3] as

$\kappa = LQ\mu / A\Delta P$ where κ is the intrinsic permeability of a sample of length L and cross-sectional area A through which a fluid flow Q is driven by an applied pressure gradient ΔP .

The dynamic fluid viscosity is μ . The permeability is conceptually simple and in cement it correlates well with other performance indicators.

The isotherm describes equilibrated systems below saturation. The approach to equilibrium requires understanding the egress and ingress of liquid water and vapour. For the capillary porosity of cement, it revolves around capillary condensation. Experimentally, the isotherm displays considerable hysteresis between drying, wetting and indeed second drying cycles.

¹ Throughout this paper, we convert values of measured and simulated permeability $k(m/s)$ to intrinsic permeability $\kappa(m^2)$ where $\kappa = k\mu / \rho g$ and μ is the dynamic fluid viscosity, ρ the density and g the acceleration due to gravity. For water at 20°C, $\kappa \sim k \cdot 10^{-7}$. This is done in order to eliminate the effects of permeation fluid. However, notwithstanding this adaptation, there is always the experimental difficulty that actual fluids may alter the cement microstructure, especially in the case of water where there may be delayed hydration.

For the first drying, literature experiments have been reviewed by Jennings [4] who explains that there is considerable observational agreement between different studies. However, the underpinning microstructural model by which this comes about remains an area of active debate. In summary, the capillary pores empty in the relative humidity (RH) range 100-85%. The gel pores follow over a wider range of RH such that by about 11% RH cement is considered to be dry, save for some residual water adsorbed on surfaces of the C-S-H. This too is removed at still lower RH. From an engineering perspective, it is the changes occurring over the middle and upper ranges of RH conditions as might correspond to many temperate parts of the world that are important. In these RH regions, it is capillary transport and condensation that is of most interest.

The permeability is less often measured in cement than in other porous media, partly because it is very low and difficult to measure reliably. Hence, there is a paucity of experimental data and as such there is considerable variability. In hydrated pastes, reported values span several orders of magnitude typically from 10^{-17} to 10^{-22} m² depending on the sample properties (e.g. chemical composition, water-to-cement ratio, hydration degree), sample preparation (e.g. drying, curing protocols), permeation fluid (e.g. water, ethanol, oxygen) and measurement method. Examples are given in Table I. While the cement in concrete structures undoubtedly suffers from microcracks, the scope of this paper is limited to the discussion of ideal cement paste without microcracks. Thus, in similar materials, we consider smaller values of permeability to be more representative of reality due to the difficulty of excluding experimental artefacts, such as micro-cracking or leakage, which tend to increase the permeability. In particular, the beam bending method that is carried out with never-dried cement notably produces some of the lowest results and we consider

these to be the best. Moreover, since samples for beam bending are less likely to be micro-cracked than samples studied by other means, the resultant permeability should be more akin to those resulting from simulation of small volumes of model pastes without micro-cracks.

TABLE I. REFERENCE PLACEHOLDERS: [5-11]

In order to explain and predict water uptake and transport in cement, a microstructural model is required. Such microstructural models have been developed for the purpose of understanding cement hydration and kinetics. Apart from getting the kinetics correct, the challenge is to work over a sufficiently broad range of length scales. The best of these models are now able to account for a range of cement properties derived from cement chemistry and thermodynamics such as phase composition, assemblage and interactions during the hydration processes. HYMOSTRUC 3D [12], CEMHYD3D [13] and μ IC [14, 15] are amongst the leading models. HYMOSTRUC 3D uses the vector approach to generate resolution-free microstructures. However, it is severely limited in so much as it grows the microstructure as expanded spheres based on the original cement particle distribution without taking into account interactions with neighbours. In so doing, it is unable to fully capture the microstructural complexity. CEMHYD3D is lattice based. Practical computer and imaging resources limit minimum particle sizes to of the order of 0.25 to 1 μ m. In consequence, generated microstructures tend to block porosity pathways at diagonal interfaces even though more complex particle shapes may be modelled than in HYMOSTRUC 3D. Like HYMOSTRUC 3D, μ IC uses the vector approach and is hence inherently resolution-free. However, additionally, it allows hydrates to nucleate in the pore space and explicitly

accounts for impingement between neighbouring grains. This leads to significant success in predicting kinetics. Also it allows more complex microstructures and a wider of pore size distribution to develop.

Within these models, a key parameter that helps determine the capillary porosity is the C-S-H density. The reason is that the density of hydrates is more than the density of the combined water and anhydrous cement from which they originate. Unfortunately, C-S-H microstructure is heterogeneous and poorly understood and determination of C-S-H density remains an active area of research [4].

Previous attempts to simulate water permeability of model cement microstructures have all followed broadly the same path. The pore network is divided into a series of nodes representing pores that are linked together by cylinders with a characteristic length and radius determined by the pore separation and throat size. The equations of laminar flow within this network of cylinders, essentially a large set of simultaneous equations, are solved. Pignat *et al.* [16] obtained intrinsic permeability values of the order of 10^{-13} to 10^{-15} m² depending on the porosity and the cement particle size distribution using the early model IKPM, a precursor of μ IC, for a water-to-cement ratio of 0.42. This result is unsurprisingly much larger than comparable experiment because the minimum cement particle size was limited to 2 μ m. Using HYMOSTRUC 3D, Ye *et al.* [17] reported simulation permeabilities varying from 10^{-18} to 10^{-20} m² between 1 and 100 days of curing for a 0.4 water-to-cement ratio paste. They noted that when they decreased the minimum simulation particle size from 2 to 1 μ m, the permeability dropped by two orders of magnitude. Related to these studies, Koster *et al.* [18] derived a sophisticated cylinder

network from 1 μm resolution 3D micro-tomographic images of cement pastes and found a permeability of $9.3 \times 10^{-20} \text{ m}^2$ for a sample with a water-to-cement ratio of 0.45 and a degree of hydration of 0.67.

To the best of our knowledge, there has as yet been no attempt to model water desorption and adsorption in any of the model microstructures. The primary reason would appear to be the difficulty of tracking the liquid / vapour interface in the complex geometry. However, to do this would be an important additional test of our understanding of cement microstructure. Indeed, to be able to model both the isotherm and permeability using a consistent approach would open the door to modelling the full range of transport phenomena that exist between these extremes.

In contrast to the preceding studies, in this work we chose to assess the lattice Boltzmann (LB) method for solving problems of fluid dynamics in the context of cement microstructure. LB has several potential advantages. First, it removes the requirement to reduce the microstructure to a network of connected cylinders. Although network models allow the computation of flows in samples larger (or with higher resolution) than is possible with LB methods, creating a network model from a structure introduces additional degrees of freedom due to the different possible means to choose the number, radius and connectivity of nodes. The use of LB avoids this difficulty and there is no inadvertent modification of the porosity. The permeability of the actual structure presented is calculated. Second, LB allows us to extend the modelling to the adsorption and desorption of water liquid and vapour as a two-phase fluid in the microstructure. In the LB approach it is not necessary to specifically track the liquid / vapour interface making it computationally efficient. This creates

opportunity to study a wide range of transport phenomena. Third, although LB is lattice based, there is the opportunity to work with a hierarchical grid with a fine resolution where needed, coarser where not. This may overcome some of the limitation of high computing resource for fine spatial resolution. In this work, we seek to exploit the first two opportunities: we have yet to attempt the third.

The LB method has previously been used to model the permeability of porous media such as rocks [19], textiles [20] and carbon paper gas diffusion layers in fuel cells [21]. It has also been used to model adsorption of fluid into real and model microstructures. For instance, Ahrenholz *et al.* [22] compared LB to a morphological pore network model and experiment for the capillary hysteresis of water uptake to, and drainage from, a sand bed. To the best of our knowledge, LB has rarely been discussed in the context of cement-based materials.

Garboczi and Bentz [23] used an LB algorithm to calculate the permeability of CEMHYD3D microstructures as a function of capillary porosity and resolution. At the highest resolution studied, the permeability ranged from circa 5×10^{-17} to $2 \times 10^{-15} \text{ m}^2$ in the capillary porosity range 12-32%. Martys and Hagedorn [24] suggested using LB for permeability estimation in cracked mortar. Svec *et al.* [25] developed a free-surface model of fibre reinforced self-compacting concrete flow during a slump test and most recently, Zhang *et al.* [26] reported ionic diffusivity in cement paste model microstructures extracted from HYMOSTRUC 3D.

In this paper, we use the LB method to calculate the permeability of microstructures determined using the model μIC as a function of water-to-cement ratio and degree of hydration of the paste. We use microstructural models, rather than actual microstructures derived from *e.g.* electron microscope images, in order to develop further pathways for the

testing of microstructural models against experimental data. We make a brief comparison with the alternate model CEMHYD3D. We also seek to use the LB method to estimate the capillary condensation part of the water adsorption / desorption isotherm for a μC structure. The contribution ends with an assessment of the current limitations of the LB method applied to cement microstructural models.

2. THEORY

2.1 The lattice Boltzmann method

The LB approach developed from the lattice gas method [27, 28] but it can also be derived from the Boltzmann equation [29]. In the LB method, the fluid is represented by a density distribution of N fluid elements each with a defined lattice velocity performing consecutive propagation and collision steps over a discrete lattice mesh. The basic LB method is encapsulated in:

$$f_i(\mathbf{r} + \mathbf{e}_i \Delta t, t + \Delta t) - f_i(\mathbf{r}, t) = \Delta t \sum_{j=1}^N S_{ij} (f_j(\mathbf{r}, t) - f_j^{eq}(\mathbf{r}, t)) + \mathbf{F}. \quad (1)$$

Here \mathbf{r} represents a lattice node, Δt is the time step and \mathbf{e}_i the allowed velocities. The functions f_i represent the density of particles moving with velocity \mathbf{e}_i at position \mathbf{r} and time t . The first term on the right hand side of Eq. (1) is the linearized collision operator in which S_{ij} is the collision matrix that serves to relax the fluid at every node towards an equilibrium distribution $f_i^{eq}(\mathbf{r}, t)$. The equilibrium distribution encapsulates the physics of the problem to be addressed. Lastly, \mathbf{F} is the external forcing term describing, for example pressure gradients, gravity, or, in multi-fluid/phase applications, interfacial tension. In the

absence of external forcing, the macroscopic density $\rho(\mathbf{r},t)$ and momentum $\rho(\mathbf{r},t)\mathbf{u}(\mathbf{r},t)$ are directly calculated from the distribution functions as:

$$\rho(\mathbf{r},t) = \sum_{i=1}^N f_i(\mathbf{r},t), \quad (2)$$

$$\rho(\mathbf{r},t)\mathbf{u}(\mathbf{r},t) = \sum_{i=1}^N f_i(\mathbf{r},t)\mathbf{e}_i, \quad (3)$$

respectively.

From this common starting point, the lattice Boltzmann method comprises a growing collection of variants developed to optimise the modelling of a particular system. Adaptation occurs at different levels. First, there is the choice of the equilibrium function that governs the physics of the problem. For the simulation of single-fluid flows, there is a standard function for the recovery of the Navier-Stokes equations [30]. Other equilibrium functions exist for the recovery of other transport equations. For more complex flows (multi-fluid and multi-phase), there are different approaches with significant differences in ease of implementation, computational costs and degree of accuracy by which they reproduce the interface dynamics and fluid thermodynamics. Second, there is the choice of the collision operator. The single-relaxation-time operator [30] is easier to implement and requires less computing resource than multi-relaxation-time operators [31] but sacrifices stability and accuracy [32]. Lastly, different means to control the flow and handle solid boundaries are available. Compromise is again required between ease of implementation, computing resource and physical reality [32]. Thus, a lattice Boltzmann algorithm may be viewed as comprising a series of “plug-ins” within a standard procedure. Care must be taken to ensure mutual compatibility of the plug-ins. Identifying an optimum combination for a

given problem is not straightforward. In developing the results that follow, we have implemented several schemes. The results we show are those that have worked best for us.

2.2 Single-fluid modelling

To simulate single-phase liquid transport in fully saturated media, the equilibrium distribution functions are:

$$f_j^{eq}(\mathbf{r}, t) = \omega_i \rho \left(1 + \frac{\mathbf{u}^* \cdot \mathbf{e}_i}{c_s^2} + \frac{(\mathbf{u}^* \cdot \mathbf{e}_i)^2}{2c_s^4} - \frac{\mathbf{u}^* \cdot \mathbf{u}^*}{2c_s^2} \right), \quad (4)$$

where the constants ω_i are lattice weights specific to the chosen lattice, \mathbf{u}^* is the equilibrium velocity equal to the macroscopic velocity in absence of external forcing, $c_s = c/\sqrt{3}$ is the lattice speed of sound where $c = \Delta x/\Delta t$ is the lattice speed and Δx the lattice spacing. Single- and multi-phase simulations were performed on a 3D, $N=19$ velocity set lattice (D3Q19) with $c=1$. The lattice weights and further details can be found in Refs. [33, 34].

For the single-phase algorithm, we implemented a multi-relaxation-time collision operator as described by D'Humières *et al.* [31]. In the notation of the reference, the relaxation rates, $s_e = s_\varepsilon = s_\pi = s_\nu = 1/\tau$ and $s_m = s_q = 8(2-s_\nu)/(8-s_\nu)$, were chosen following the two-relaxation-time model [32, 35]. The time constant τ is related to the kinematic fluid viscosity ν through $\nu = c_s^2(\tau - \Delta t/2)$. An advantage of the multi- compared to single-relaxation-time collision operator is that the effective locations of the wall are viscosity independent with standard bounce-back at solid interfaces [32]. We use $\tau = 0.6$ following the work of Ref. [36]. The pressure gradient driving the fluid was simulated with an external

force $F_i = 3\omega_i\rho_0\mathbf{e}_i \cdot \mathbf{g}$ [37] where ρ_0 is the mean density (set to 1) and \mathbf{g} the acceleration due to external forces. No injection chambers were needed because the microstructures generated with μIC have periodic boundary conditions. When a constant body force is applied throughout the sample, it is not necessary to calculate the pressure gradient because its value is simply given by \mathbf{g} [38].

2.3 Multi-phase modelling

For the study of adsorption / desorption isotherms, a multi-phase algorithm is required, so as to properly describe the liquid-water and vapour and the interface between them without formally tracking the interface or treating them as two distinct fluids (such as air and water). We chose to implement the free energy model proposed by Swift *et al.* [39] and advanced in Refs. [40-42]. Directly following these authors, the pressure tensor describing the fluid is written

$$P_{\alpha\beta} = \xi \left[\left(p_0 - \chi\rho\nabla^2\rho - \frac{\chi}{2}|\nabla\rho|^2\delta_{\alpha\beta} + \chi\partial_\alpha\rho\partial_\beta\rho \right) \right]. \quad (5)$$

Here p_0 is the bulk liquid pressure. The other terms, dependent on the free parameter χ describe the liquid / vapour interface. The pressure is scaled by a factor ξ to improve numerical stability following Ref. [42]. We use a van der Waals gas to describe the water, for which the equation of state, in reduced units at temperature $\theta = 1/3$ is written

$$p_0 = \frac{\rho}{3-\rho} - \frac{9}{8}\theta_c\rho^2 \quad \text{where the critical temperature and density are } \theta_c \text{ and } \rho_c = 1$$

respectively. According to this model, the equilibrium distributions are:

$$f_j^{eq}(\mathbf{r}, t) = \omega_i \left\{ \frac{\rho}{c_s^2} (\mathbf{e}_i \cdot \mathbf{u}) + \frac{3\rho}{2c_s^4} (\mathbf{e}_i \cdot \mathbf{u})^2 - \frac{\rho}{2c_s^2} (\mathbf{u} \cdot \mathbf{u}) + \frac{3}{2c_s^4} \lambda [2(\mathbf{e}_i \cdot \mathbf{u})(\mathbf{e}_i \cdot \nabla \rho) + (\mathbf{e}_i \cdot \mathbf{e}_i)(\mathbf{u} \cdot \nabla \rho)] - \frac{3}{2c_s^2} \lambda (\mathbf{u} \cdot \nabla \rho) \right\} + \frac{1}{c_s^2} \left(\omega_i^p p_0 - \omega_i^t \rho \nabla^2 \rho + \sum_{\alpha=x,y,z} \omega_i^{\alpha\alpha} \chi \partial_\alpha \rho \partial_\alpha \rho + \sum_{\alpha,\beta=x,y,z; z;x} \omega_i^{\alpha\beta} \chi \partial_\alpha \rho \partial_\beta \rho \right). \quad (6)$$

The lattice weights ω_i are given in Ref. [40]. The term involving the parameter

$\lambda = (\tau - 1/2) \left(3 - \frac{dp_0}{d\rho} \right)$ ensures Galilean invariance [40]. For the multi-phase algorithm, we

implemented the single-relaxation-time collision operator which reduces the collision matrix to $S_{ij} = -\delta_{ij}/\tau$ and we let the system equilibrate in the absence of external forces.

The surface tension depends on χ as described in the references. In practice, the dependence is complex, but it may be calibrated by running small test simulations comprising a liquid drop in vapour and measuring the pressure difference across the interface (Young-Laplace equation). The contact angle with solid boundaries is dependent on the surface-normal fluid-density gradient, which is maintained constant at solid interfaces, again as described in the references. Once more, the relationship is complex but may be calibrated with test simulations of liquid drop on a surface.

For both the single- and multi-phase algorithms, the no-slip fluid-solid boundary condition [43] was simulated by applying the standard bounce-back rule: if a fluid element hits a boundary after the propagation step, its momentum is reversed.

3. IMPLEMENTATION

The LB algorithm is amenable to parallelization and may be so implemented on modern graphics processing units (GPU) that contain hundreds of stream processors. We implemented it in MATLAB[®] using Jacket[®] [44, 45] GPU engines capable of running on any computer equipped with a CUDA[™]-enabled GPU. The system used to run the simulations comprises an NVIDIA GeForce[®] GTX 460M with 192 CUDA[™] cores running at 1.36 GHz and 1.5 GB of memory. Using Jacket, we achieved a speedup (execution time on CPU / execution time on GPU) of 15.8 for systems with 1 million nodes. Typical single-phase simulations shown in the results section take few hours to converge depending on the connectivity and the characteristic size of the pores in the system.

4. VALIDATION

4.1 Validation of the single-phase fluid model

To validate the single-phase model, we compared the numerical and theoretical permeabilities, as defined by Darcy's law, for a flow between two parallel plates with a constant cross section [46]. We considered the simulation converged when the mean velocity change per voxel per time step averaged over 100 time steps was less than 1 part in 10^8 . The relative error in permeability $\varepsilon(\kappa) = \left| \kappa^{LB} - \kappa^{theory} \right| / \kappa^{theory}$ decreases from 36% for a 1-node-wide channel, to 1.4% for 10 nodes and to less than 0.1% for 40 nodes.

To test the accuracy of the model in a more complicated geometry, we computed the flow past a cubic array of overlapping spheres of radius r and centre-to-centre spacing L . We

varied the lattice resolution while keeping the porosity at circa 20%. The permeability is

given by $\kappa^{theory} = \frac{1}{6\pi C_D} \frac{L^3}{r}$ where C_D is the porosity dependent drag force coefficient as

described in Ref. [47]. Figure 1 shows the relative error in permeability as a function of the size of the system. With increasing resolution, the error decreases and the calculated permeability converges to the theoretical value. However, the error does not decrease monotonically, presumably due to the discretization of the spheres as has been previously observed in Ref. [48].

In a further test, we computed the permeability of a cubic array of spheres as a function of τ (and hence fluid viscosity) from $\tau = 0.6$ to 2.0 and confirmed that the permeability has very small dependence on viscosity, a clear advantage of the multi-relaxation-time collision operator [32].

4.2 Validation of the multi-phase fluid model

For the validation of the multi-phase model, we investigated phase separation, liquid / vapour interface tension and the pressure drop across curved interfaces (Young-Laplace equation), contact angle at solid surfaces, capillary rise (Washburn equation), and the formation of pendular rings between packed spheres. In particular, we confirmed that the contact angle varies approximately linearly with the surface normal fluid density [41] (Fig. 2(a)) and that the pressure decrease across a liquid drop interface varies inversely with the radius (Fig. 2(b)). The simulated interfacial tension, evaluated by direct integration across an interface [49] is within 6% of that found from the gradient of the best fit line to the plot. For

the case of capillary rise, we implemented a system comprising a liquid reservoir maintained full by a liquid source coupled to a large vapour reservoir by a capillary and saw that the liquid rose in the capillary with the square root of time (Fig. 2(c)). For $\theta/\theta_c = 0.95$, and without a periodic boundary condition between the two reservoirs, we do not observe the significant condensation of the liquid from the vapour in the capillary that speeds the apparent transport as has been reported elsewhere [50]. Finally, we observed the condensation of pendular rings of liquid between the near points of a cubic array of liquid wetting spheres at reduced vapour pressures (Fig. 2(d)). The above simulation tests were carried out mainly for reduced fluid temperature in the range 0.80 to 0.96 with pressure scaling factors ranging from 0.005 to 0.8. A small number of test simulations were carried out at lower reduced temperatures and hence greater liquid to vapour density ratios. However, these were extremely slow to run on reasonably sized systems (given the very small pressure scaling factor required) and tended to be stable in complex geometries only if the starting conditions were near equilibrium.

5. CEMENT MODEL MICROSTRUCTURES

We obtained model microstructures using the μ IC model [14, 15]. Structures were generated with water-to-cement (w/c) ratios ranging from 0.3 to 0.7 as a function of degree of hydration. The smallest and largest anhydrous particle sizes were set to 0.25 and 18 μm respectively. The model cement clinker comprised 69% alite, 10% belite, 8% ferrite, 7% aluminate, and 6% gypsum by solid volume. The reaction kinetics were defined according to Rietveld analysis results reported in Ref. [51] for a similar cement composition. The reactant and hydrate (except C-S-H) densities were set following Ref. [52]. Calculations based on the

Powers-Brownyard model [53] as reported by Taylor [54], predict that for a water-to-cement ratio of 0.4 at 85 and 95% degree of hydration, the capillary porosity is 10.7 and 5.4%, respectively. In order to match these porosities within μIC , the density of C-S-H was set to $\rho_{\text{C-S-H}} = 1.965 \text{ g/cm}^3$. Generated structures were subsequently translated onto a cubic grid with a lattice spacing of 0.25, 0.5 or 1 μm as required by taking the phase present at the voxel centre as representative of the voxel. The simulation volumes comprised up to 100^3 voxels. Throughout this work, all solids phases, including C-S-H, were treated as impermeable solid with no inherent porosity and ascribed the same surface properties (e.g. contact angle with water).

Figure 3 shows the pore size distribution of a μIC -generated cement sample with water-to-cement ratio of 0.4 at 0 and 85% degree of hydration. The capillary porosity has a significantly larger fraction of large pores than is typically measured in cement (e.g. by mercury intrusion porosimetry). This is partly a resolution issue associated with the transfer of μIC output to a lattice grid.

Finally, in order to investigate the effect of the microstructural model on water transport, and to compare our results with those of Ref. [23], we obtained a single CEMHYD3D cement microstructure [13] that mimicked the lowest porosity μIC structure used. The structure is based on the Cement and Concrete Reference Laboratory Cement 152 and comprised 73.44% alite, 9.38% belite, 4.07% ferrite and 13.11% aluminate by solid volume [55]. The water-to-cement ratio is 0.4, the hydration degree 93.5% and the capillary porosity 10.58%.

We note that at low porosity and with a 1 μm resolution, both μIC and CEMHYD3D microstructures are below percolation threshold, an observation that is discussed further in section 6.1.4.

For permeability calculations, cement microstructures were generated with periodic boundary conditions. For adsorption simulations, test microstructures were extracted from a larger system.

6. APPLICATION TO MODEL CEMENT MICROSTRUCTURES

6.1 Single-phase modelling

6.1.1 Reproducibility of the computed permeability

At the start of each structure determination, given an anhydrous particle size distribution, μIC randomly generates the initial position of the reactant particles. The result is a unique, randomly generated microstructure. To test the reproducibility of the simulated permeability, we computed the flow in multiple test microstructures generated from different initial configurations. The resulting microstructures have similar porosities ($\pm 0.1\%$) and the corresponding computed permeabilities have a normalized standard deviation (standard deviation / average permeability value) below 2%. We also tested the isotropy of the samples by computing the permeability in each of the three spatial directions. The standard deviation is again less than 2%. Finally, the permeability was seen to be independent of the applied pressure gradient.

6.1.2 Permeability of cement microstructures

The permeability was computed for μC microstructures spanning the full range of tested degrees of hydration and water-to-cement ratios. We consider the simulation converged when the convergence rate, as defined in section 4.1, becomes smaller than 1 part in 10^6 or after 500,000 lattice time steps. This latter criterion was only required for porosities less than 11%. In the worst case, convergence was better than 1 part in 10^4 . The results are shown in Figures 4 and 5 for a structure with $1\ \mu\text{m}$ lattice spacing.

The size distribution and connectivity of the pores determines the permeability. In cement, on the one hand, the greater the initial water-to-cement ratio, the smaller the fraction of space occupied by hydrates, and hence the greater the permeability. On the other hand, the greater the degree of hydration, the greater the solid volume fraction and consequently the smaller the permeability. The permeability evolution can be divided into 2 regimes: above and below 20% porosity. Above 20% porosity, the simulated permeabilities of all 4 water-to-cement ratio systems tested show similar behaviour. The permeabilities decrease exponentially with the degree of hydration and with broadly similar rate constants. Below 20% porosity (w/c 0.3 and 0.4), the permeability decrease is noticeably sharper. In part, we attribute this latter dependence to depercolation of the pore network.

In all of the above, the computed permeability is larger than expected from experiments (Table I). Three factors contribute to this: the fact that minimum feature size is one pixel wide, the limited spatial resolution of the microstructure and the influence of diagonal leaks

in the lattice Boltzmann method. A further issue is the existence / absence of micro cracks in real / model systems. These topics are addressed in the following sections.

6.1.3 Model resolution and scaling

In well hydrated cement model structures, a large fraction of the pores have a diameter of 1 pixel (which in the previous simulations equated to 1 μm). As demonstrated in the Poiseuille flow test, the permeability is overestimated by 36% in 1-node-wide channels. To avoid permeability overestimation and to recover correct hydrodynamics, the microstructure pore channels should have a minimum width of 4 nodes as discussed by Succi [56]. Otherwise, in complex geometries, the overestimation errors do not necessarily cancel and can add up to produce permeabilities several order of magnitude too big. To guarantee a minimum of 4 nodes, the lattice resolution may be increased 4 times in each of the 3 spatial directions without changing the inherent resolution and morphology of the microstructure, simply by dividing every voxel into 4^3 smaller voxels. The resulting lattice is 64 times larger: we term this “lattice magnification” by a factor 4.

In parallel to the lattice magnification, the microstructure should be generated at the highest possible resolution. Since μIC is resolution-free, the resolution limit derives from the discretization of the microstructure, and thus from the computational resources available to run the LB algorithms. This is microstructure resolution.

To investigate the combined effects of the lattice magnification and microstructure resolution, we computed the permeability of a 65% hydrated μIC cement with a water-to-

cement ratio of 0.4 for several structural resolutions (1, 0.5 and 0.25 μm) and lattice magnifications (1, 2 and 4). The porosity was kept at circa 21.5%. Table II shows the computed permeability for different microstructure resolutions and lattice magnifications.

As expected, magnification of the porous medium artificially widens the channels, allowing the LB algorithm to better recover correct hydrodynamics. The permeability decreases as expected and as previously observed in Refs. [19, 36]. Also, reducing the microstructure pixel size results in a larger number of small solid particles being resolved. The structural complexity is increased. The minimum pore diameter and thus the permeability is decreased. This too may have been expected and was previously observed in Refs. [9, 23]. What is less expected is that both actions result in similar scaling of the permeability and that the effects are multiplicative. At lower porosities, the magnification enhancement still applies, but the permeability dependence on the structural resolution becomes smaller, and is un-measurable within the simulation variability/noise.

6.1.4 *Diagonal leaks*

At around 10% porosity, and with a 1 μm resolution, the μC pore structure is depercolated. The reason that we can calculate a permeability below percolation threshold is that LB allows “diagonal leaks”. Diagonal leaks allow fluid to pass between neighbouring lattice points with a single edge in common. Indeed, Manwart *et al.* [48] reported a non-zero permeability for a non-percolating three-dimensional checker-board structure. At higher porosities, diagonal leaks play a far smaller role in the overall connectivity. If better accuracy is required for structures near percolation threshold, diagonal leaks can be eliminated by

applying the bounce-back rule at these edges [48]. In all the computations carried out in this work, but especially at low porosity, diagonal leaks have effectively increased the pore connectivity and hence the computed permeability. It seems probable that they effectively compensate for the lack of fine porosity caused by low resolution in the structures used for lattice Boltzmann simulations.

6.1.5 Microcracks

To a greater or lesser extent, all real microstructures have microcracks that serve to increase the measured permeability. Model structures such as we have used do not, and so the discrepancy between experiment and model permeability may be larger than at first apparent. On the scale of the model structures used, it is unrealistic to impose cracks in a meaningful manner. In mitigation, we simply note that we chose to compare model data to experimental data for which we believe micro cracking to have the smallest impact: that obtained on never-dried material by beam bending methods [8].

6.1.6 Comparison of μ IC and CEMHYD3D

It is interesting to compare the permeability calculated for μ IC in Figure 5 with that found for CEMHYD3D by Garboczi and Bentz [23]. Taking data at the same physical resolution (1 μ m) and lattice size (100^3) from their figure 14, Garboczi and Bentz report $\kappa = 8 \times 10^{-15}$ and $6 \times 10^{-15} \text{ m}^2$ at 28 and 26% capillary porosity, respectively. This is in good agreement with the permeabilities computed for μ IC in this work of 7×10^{-15} and 4.4×10^{-15} at 27.4 and 24.1%

capillary porosity, respectively. This good agreement, however, diminishes as the capillary porosity is reduced as will be seen below.

We compare the μ IC and CEMHYD3D microstructures with low porosities at 10.64 and 10.58% respectively. The calculated permeability for the μ IC structure is $1.62 \times 10^{-18} \text{ m}^2$ and for the CEMHYD3D structure is $4.67 \times 10^{-17} \text{ m}^2$ without scaling or magnification. Very clearly, while the porosities of the μ IC and CEMHYD3D microstructures are very similar, the permeability of the μ IC microstructure is one order of magnitude smaller and much closer to the range of experimental observations. This is clearly in contrast to the comparison at higher porosity (24-28%) where the permeabilities were very similar. One of the possible reasons for this discrepancy is the difference in pore size distribution of the two microstructures. CEMHYD3D has a significantly larger number of bigger pores compared to μ IC. Also, CEMHYD3D has a slightly (+10%) larger number of diagonal leaks.

6.2 Multi-phase modelling

6.2.1 Liquid / vapour density ratios

A key difficulty in liquid / vapour LB methods is satisfactorily modelling a large density ratio. Wagner and Pooley 2007 [42] have shown how large pressure differences corresponding to a low temperature can be achieved by introducing a pressure scaling factor and by softening (in terms of the number of pixels) the interface between the liquid and vapour. The cost is a very large (even prohibitive) increase in the requisite computation time. However, since we

are interested in quasi-equilibrium fluid distributions, it is possible to obtain useful results at much higher simulation temperatures (and hence lower pressure differences).

As an example, Fig. 6 shows the equilibrium phase distribution of fluid in a single cement pore obtained at 3 different reduced temperatures θ/θ_c (liquid : vapour density ratios) of 0.95 (2.3 : 1); 0.8 (8.1 : 1) and 0.5 (113 : 1) respectively for a constant bulk liquid volume fraction of 2/3. The microstructure resolution is the same in each case but the linear pixel size varies by a factor of 0.1 between the first and last. The computation time increases by a factor of approximately 10,000. The key observation, however, is that the essential fluid distribution is similar for the 3 temperatures.

6.2.2 Equilibrium distributions in the absence of macroscopic transport

The LB multi-phase algorithm is used to find the equilibrium distribution of water within a 2D μIC segment of 200^2 pixels for $\theta/\theta_c = 0.95$, $\chi = 0.059$ and a solid surface normal fluid density $d\rho/ds = 0.2$ yielding a nominal contact angle $\phi_c = 16^\circ$. The choice of χ corresponds to a bulk fluid liquid / vapour interface width of about 1.5 pixels. A pressure scaling factor of $\xi = 0.5$ is used to ensure that the simulation is stable. It does not affect the final liquid / vapour distribution. The simulation is begun from an initial liquid density in all porosity of $\rho_{initial} = \rho_{gas} + (\rho_{liquid} - \rho_{gas})/3$ where $\rho_{gas:liquid}$ are the bulk phase (reduced) densities: in this case $\rho_{gas} = 0.58$ and $\rho_{liquid} = 1.46$. This corresponds to one third liquid, two third gas by volume in a homogenous space. The simulation was run for 1 million time steps after which the density per pixel per iteration averaged over all pixels for 250

iterations was stable to nearly 1 part in 10^6 . Only very minor differences in occasional pixels were seen in the liquid and vapour distributions after 1 million cycles (Fig. 7) compared to 1/3 million cycles. We suggest that this distribution corresponds closely to that which might be expected for the same liquid fraction in a real system equivalent to the model system left without further hydration for times corresponding to geological ages.

6.2.3 Adsorption / desorption isotherms

In practice, in cement, the very long term distribution may not be achieved except perhaps in sealed-cured materials that undergo shrinkage during hydration leading to the microscopic *in-situ* creation of partially filled capillary porosity. More normally, cement is exposed to the environment and thus to changes in ambient relative humidity.

To see how liquid distribution changes in the case of adsorption and desorption, a 3D μ IC segment has been equilibrated while in contact with a vapour of constant relative humidity, initially 100%. The simulation parameters are $\theta/\theta_c = 0.96$, $\chi = 0.0104$ and a solid surface normal fluid density $d\rho/ds = 0.264$. The porosity is 22%. The simulation was run 5 times for microstructures with different sample volumes of $72 \times 72 \times 18$ and $64 \times 30 \times 30$ at a resolution of $(0.5 \mu\text{m})^3$ and lattice magnification 2. These parameters lead to a nominal liquid / vapour interface width of 1 pixel and a contact angle of $\phi_c = 45^\circ$ and to bulk liquid and vapour densities of $\rho_{gas} = 0.62$ and $\rho_{liquid} = 1.41$ respectively. Once equilibrated, the surrounding vapour pressure is progressively reduced in steps of $\frac{1}{3}\%$ and the system re-equilibrated until there is no liquid left in the structure after which the vapour pressure is

progressively increased again. In this way, a complete adsorption / desorption isotherm is modelled. At each vapour stage, the system is equilibrated so that the average density varies by no more than 5 parts in 10^6 in each voxel per iteration averaged over 2000 iterations. Running multiple, smaller simulations is preferred to running a single, large simulation since it allows us to estimate the scatter associated with the calculated isotherms and also since the simulations converge more quickly due to the need to transport water across the structure. The structures were chosen to be cumulatively as representative of the total as possible.

The complete adsorption / desorption isotherm is shown in Fig. 8. The shaded region shows the variation (standard error in the mean) in the multiple simulations. The isotherm shows considerable hysteresis. The mass of adsorbed liquid can be computed as the sum of the distribution functions f_i in pores containing liquid, or as the number of pores containing liquid. For deeply quenched liquids these are essentially the same. At greater reduced temperatures, they differ slightly due to the compressibility of the liquid. In figure 8, the adsorbed liquid is calculated as the sum of the distribution functions in pores containing liquid so that at 100% RH the mass of adsorbed liquid is equivalent to the liquid density, ρ_{liquid} . Within the scatter, the differences between the two methods cannot be resolved (not shown in the figure).

An exemplar pair of next neighbour slices from the structure around critical vapour pressures are shown in Fig. 9. A macro-surface layer of water resides on both the sample surfaces in contact with the vapour down to about 98.3% RH and on one only down to 96.0% RH on the desorption path. This layer was not included in the calculations of the

isotherms shown in Fig. 8. The average desorption isotherm shows a number of steps at which pores of a specific size empty. Small pore throats retain water down to 87% RH at which point they dry and the water in larger pores behind rapidly follows. On the adsorption path branch, these pores do not refill until circa 96% RH. The macro-surface layer is not recovered until 100%. The simulations show that there are a handful of unconnected pores which do not empty. These account for about 1% of the test-volume porosity. Although the simulations suffers from a small structure matrix size, the results capture the broad features of the capillary part of the desorption isotherm as reported in literature [4].

7. DISCUSSION AND CONCLUSIONS

In general, the lattice Boltzmann method captures the essential features of experimentally measured permeability. However, for the bulk of our results, the computed permeability is systematically larger than that derived from measurements with water. The permeability is critically dependent on the porosity which is dependent on the C-S-H density. At the current time, accurate determination of the density of C-S-H remains a point of discussion. It is thought to be dependent on many factors, including the sample history. Jennings [4] has reviewed the literature and proposed a colloidal model that seeks a consistent picture across the full water sorption range. In part the issue surrounds the assignment of porosity either to nano-scale pores or larger capillary pores. Increasingly, there is nuclear magnetic resonance evidence for smaller fractions of capillary porosity than traditionally thought [57]. Fewer capillary pores place a greater fraction of the water in the gel porosity and hence reduce its density.

With the exception of the small particle analysis of Ye *et al.* [17], our results are as good as, or better, than previous studies based on model microstructures when compared to experiment. In the case of Ye *et al.*, however, the extent to which choices made in the creation of the network model from the microstructure influenced the result is unknown. In particular, we find that for μ IC and CEMHYD3D microstructures with similar large porosity, μ IC yields a similar permeability to CEMHYD3D. However, the μ IC permeability is significantly smaller at lower porosity, closer to experimental observations.

Ye *et al.*'s work, and our own scaling study, illustrate that the spatial resolution of the model microstructure is critically important. Almost certainly, at the scales at which we have so far worked, we overestimate the number of larger pores in the pore size distribution and underestimate the smaller pores. Indeed, it is known from experiment that there is normally a substantial reservoir of pores smaller than 0.25 μ m in cement pastes. There are three issues. The first is to satisfactorily exploit within an LB simulation the inherent resolution-free character of the model μ IC at its current stage of development. The difficulty is one of computing resources, a problem that may become prohibitive. The second is the inability of the microstructural models to capture the pore break-through diameter [58] which is probably the most critical factor in determining permeability. Third, there is an immediate limitation of all the structure generation codes, which currently do not reveal the intrinsic porosity and microstructure of the C-S-H. The contribution of the C-S-H porosity (the gel porosity) to the macro permeability has not yet been made quantitative although there are indications that it may be significant. For instance, some reported values of the tortuosity of cement pore networks inferred from experiment are extremely high, in excess of 100 [59]. It may yet prove to be the case that the capillary porosity of all models lacks complexity and

fineness that is in part compensated by additional connectivity provided by gel porosity in measurements of permeability and also, at the current stage of development, by diagonal leaks in the lattice Boltzmann method. In future work, it may be possible to include the C-S-H as an effective medium as proposed in Refs [60, 61] or by artificially increasing its viscosity in a manner comparable to that which has been done for, *e.g.*, biofilms [62].

Similar comments apply to the adsorption / desorption data. Cement isotherms have been published by many authors including Refs. [4, 63]. Here the issue of limited scale and of the absence of gel porosity within the C-S-H is clear. In the modelled isotherms, hysteresis loops appear indicating the occurrence of capillary condensation. However, the lack of breadth to the capillary pore size distribution, and in particular to the pore throat distribution, leads to an isotherm with a dramatic desorption step at around 90% RH. The absence of resolution of the C-S-H gel porosity within the microstructural models leads to the false conclusion that the porosity is empty by circa 80% RH. This nano-scale porosity is known to be extremely important to cement properties, but is only poorly understood experimentally. The density ratio of the vapour and liquid is a further issue. Hence, while the LB model can qualitatively reproduce the early part of the adsorption isotherm related to the capillary porosity, considerable work is required to parameterise LB with sufficient accuracy for it to adequately model experiment.

In conclusion, we believe that the LB method holds much promise for the study of water transport in cementitious materials and that it may yet prove to be an important discriminator between different microstructural models, as we have seen with μ IC and CEMHYD3D. Its application to mortars and concretes with larger fractions of larger pores

may be more rapid than its advance in studying cement paste however. In particular, the latter requires work both in terms of microstructural models and in terms of computing efficacy to adequately describe the C-S-H gel porosity, perhaps by assignment of the C-S-H as an effective medium with effective properties.

ACKNOWLEDGEMENTS

We thank Karen Scrivener (Ecole Polytechnique Fédérale de Lausanne, Switzerland) for helpful discussions, Shashank Bishnoi (Indian Institute of Technology, India) for providing the μC microstructures and Sébastien Rémond (Ecole des Mines de Douai, France) for providing the CEMHYD3D microstructure used in this work. The research leading to these results has received funding from the European Union Seventh Framework Programme (FP7 / 2007-2013) under grant agreement 264448. PJM thanks Nanocem (www.nanocem.org) and the UK Engineering and Physical Sciences Research Council (grant number: EP/H033343/1) for financial support.

References

- [1] E. Gartner, Industrially interesting approaches to “low-CO₂” cements, *Cem Conc Res*, 34 (2004) 1489-1498.
- [2] World Business Council for Sustainable Development, Cement Sustainability Initiative, <http://www.wbcdcement.org>, (accessed 1st December 2011).
- [3] H. Darcy, *Les Fontaines Publiques de la Ville de Dijon*, Dalmont, Paris, 1856.
- [4] H.M. Jennings, Refinements to colloid model of C-S-H in cement: CM-II, *Cem Conc Res*, 38 (2008) 275-289.
- [5] T.C. Powers, L.E. Copeland, J.C. Hayes and H.M. Mann, Permeability of Portland cement paste, Portland Cement Association (Bulletin 22), Michigan (1955), reprinted from *Proc. J. Am. Concr. Inst.* 51 (1954), p. 285-298.
- [6] B.K. Nyame and J.M. Illston, Relationships between permeability and pore structure of hardened cement paste, *Mag Concrete Res*, 33 (1981) 139-146.
- [7] N. Banthia and S. Mindess, Water permeability of cement paste, *Cem Conc Res*, 19 (1989) 727-736.
- [8] W. Vichit-Vadakan and G.W. Scherer, Measuring Permeability of Rigid Materials by a Beam-Bending Method: III, Cement Paste, *J Am Ceram Soc*, 85 (2002) 1537-1544.
- [9] G. Ye, Percolation of capillary pores in hardening cement pastes, *Cem Conc Res*, 35 (2005) 167-176.
- [10] Z.C. Grasley, G.W. Scherer, D.A. Lange and J.J. Valenza, Dynamic pressurization method for measuring permeability and modulus: II. cementitious materials, *Mater Struct*, 40 (2007) 711-721.

- [11] H.S. Wong, M. Zobel, N.R. Buenfeld and R.W. Zimmerman, Influence of the interfacial transition zone and microcracking on the diffusivity, permeability and sorptivity of cement-based materials after drying, *Mag Concrete Res*, 61 (2009) 571 –589.
- [12] K. van Breugel, Numerical simulation of hydration and microstructural development in hardening cement-based materials (I) theory, *Cem Conc Res*, 25 (1995) 319-331.
- [13] D.P. Bentz, Three-Dimensional Computer Simulation of Portland Cement Hydration and Microstructure Development, *J Am Ceram Soc*, 80 (1997) 3-21.
- [14] S. Bishnoi, Vector modeling of hydrating cement microstructure and kinetics, Ph.D. thesis, Ecole Polytechnique Fédérale de Lausanne, 2008.
- [15] S. Bishnoi and K.L. Scrivener, μic : A new platform for modelling the hydration of cements, *Cem Conc Res*, 39 (2009) 266-274.
- [16] C. Pignat, P. Navi and K.L. Scrivener, Simulation of cement paste microstructure hydration, pore space characterization and permeability determination, *Mater Struct*, 38 (2005) 459-466.
- [17] G. Ye, P. Lura and K. van Breugel, Modelling of water permeability in cementitious materials, *Mater Struct*, 39 (2006) 877-885.
- [18] M. Koster, J. Hannawald and W. Brameshuber, Simulation of water permeability and water vapor diffusion through hardened cement paste, *Comput Mech*, 37 (2006) 163-172.
- [19] B. Ferréol and D.H. Rothman, Lattice-Boltzmann simulations of flow through Fontainebleau sandstone, *Transport Porous Med*, 20 (1995) 3-20.
- [20] E.B. Belov, S.V. Lomov, I. Verpoest, T. Peters, D. Roose, R.S. Parnas, K. Hoes and H. Sol, Modelling of permeability of textile reinforcements: lattice Boltzmann method, *Compos Sci Technol*, 64 (2004) 1069-1080.

- [21] L. Hao and P. Cheng, Lattice Boltzmann simulations of anisotropic permeabilities in carbon paper gas diffusion layers, *J Power Sources*, 186 (2009) 104-114.
- [22] B. Ahrenholz, J. Tölke, P. Lehmann, A. Peters, A. Kaestner, M. Krafczyk and W. Durner, Prediction of capillary hysteresis in a porous material using lattice-Boltzmann methods and comparison to experimental data and a morphological pore network model, *Adv Water Resour*, 31 (2008) 1151-1173.
- [23] E.J. Garboczi and D.P. Bentz, The effect of statistical fluctuation, finite size error, and digital resolution on the phase percolation and transport properties of the NIST cement hydration model, *Cem Conc Res*, 31 (2001) 1501-1514.
- [24] N.S. Martys and J.G. Hagedorn, Multiscale modeling of fluid transport in heterogeneous materials using discrete Boltzmann methods, *Mater Struct*, 35 (2002) 650-658.
- [25] O. Švec, J. Skoček, H. Stang, J.F. Olesen and P.N. Poulsen, Flow simulation of fiber reinforced self-compacting concrete using lattice Boltzmann method, Abstracts and Proceedings in International Congress on the Chemistry of Cement, Madrid, 2011, edited by A. Palomo, A. Zaragoza, J.C. Lopez Agui, (ISBN: 978-84-7292-400-0).
- [26] M. Zhang, G. Ye and K. van Breugel, Lattice Boltzmann simulation of the ionic diffusivity of cement paste, Abstracts and Proceedings in International RILEM Conference on Advances in Construction Materials Through Science and Engineering, Hong Kong, 2011, edited by C. Leung, K.T. Wan, (ISBN: 978-2-35158-116-2).
- [27] G.R. McNamara and G. Zanetti, Use of the Boltzmann Equation to Simulate Lattice-Gas Automata, *Phys Rev Lett*, 61 (1988) 2332-2335.
- [28] F.J. Higuera and J. Jiménez, Boltzmann Approach to Lattice Gas Simulations, *Europhys Lett*, 9 (1989) 663-668.

- [29] X. He and L.-S. Luo, Theory of the lattice Boltzmann method: From the Boltzmann equation to the lattice Boltzmann equation, *Phys Rev E*, 56 (1997) 6811-6817.
- [30] H. Chen, S. Chen and W.H. Matthaeus, Recovery of the Navier-Stokes equations using a lattice-gas Boltzmann method, *Phys Rev A*, 45 (1992) 5339-5342.
- [31] D. D' Humières, I. Ginzburg, M. Krafczyk, P. Lallemand and L.-S. Luo, Multiple-relaxation-time lattice Boltzmann models in three dimensions, *Philos Trans Roy Soc Lond A*, 360 (2002) 437-451.
- [32] C. Pan, L.-S. Luo and C.T. Miller, An evaluation of lattice Boltzmann schemes for porous medium flow simulation, *Comp Fluids*, 35 (2006) 898-909.
- [33] D. Raabe, Overview of the lattice Boltzmann method for nano- and microscale fluid dynamics in materials science and engineering, *Model Simul Mater Sc Eng*, 12 (2004) 13-46.
- [34] J.M. Yeomans, Mesoscale simulations: Lattice Boltzmann and particle algorithms, *Physica A*, 369 (2006) 159-184.
- [35] D. D' Humières and I. Ginzburg, Viscosity independent numerical errors for Lattice Boltzmann models: From recurrence equations to "magic" collision numbers, *Comput Math Appl*, 58 (2009) 823-840.
- [36] A. Narváez, T. Zauner, F. Raischel, R. Hilfer and J. Harting, Quantitative analysis of numerical estimates for the permeability of porous media from lattice-Boltzmann simulations, *Journal of Statistical Mechanics: Theory and Experiment*, 2010 (2010) P11026.
- [37] Z. Guo, C. Zheng and B. Shi, Discrete lattice effects on the forcing term in the lattice Boltzmann method, *Phys Rev E*, 65 (2002) 046308.
- [38] A. Narváez and J. Harting, Evaluation of pressure boundary conditions for permeability calculations using the lattice-Boltzmann method, *Adv Appl Math Mech*, 2 (2010) 685-700.

- [39] M.R. Swift, E. Orlandini, W.R. Osborn and J.M. Yeomans, Lattice Boltzmann simulations of liquid-gas and binary fluid systems, *Phys Rev E*, 54 (1996) 5041-5052.
- [40] C.M. Pooley and K. Furtado, Eliminating spurious velocities in the free-energy lattice Boltzmann method, *Phys Rev E*, 77 (2008) 046702.
- [41] C.M. Pooley, H. Kusumaatmaja and J.M. Yeomans, Contact line dynamics in binary lattice Boltzmann simulations, *Phys Rev E*, 78 (2008) 056709.
- [42] A.J. Wagner and C.M. Pooley, Interface width and bulk stability: Requirements for the simulation of deeply quenched liquid-gas systems, *Phys Rev E*, 76 (2007) 045702.
- [43] X. He, Q. Zou, L.-S. Luo and M. Dembo, Analytic solutions of simple flows and analysis of nonslip boundary conditions for the lattice Boltzmann BGK model, *J Stat Phys*, 87 (1997) 115-136.
- [44] AccelerEyes, <http://www.accelereyes.com>, (accessed 1st December 2011).
- [45] K.R. Tubbs and F.T.-C. Tsai, GPU accelerated lattice Boltzmann model for shallow water flow and mass transport, *Int J Numer Meth Eng*, 86 (2011) 316-334.
- [46] T.W. Patzek and D.B. Silin, Shape Factor and Hydraulic Conductance in Noncircular Capillaries: I. One-Phase Creeping Flow, *J Colloid Interf Sci*, 236 (2001) 295-304.
- [47] R.E. Larson and J.J.L. Higdon, A periodic grain consolidation model of porous media, *Phys Fluids A*, 1 (1989) 38-46.
- [48] C. Manwart, U. Aaltosalmi, A. Koponen, R. Hilfer and J. Timonen, Lattice-Boltzmann and finite-difference simulations for the permeability for three-dimensional porous media, *Phys Rev E*, 66 (2002) 016702.
- [49] A.J. Briant, P. Papatzacos and J.M. Yeomans, Lattice Boltzmann Simulations of Contact Line Motion in a Liquid-Gas System, *Philos Trans Roy Soc Lond A*, 360 (2002) 485-495.

- [50] C.M. Pooley, H. Kusumaatmaja and J.M. Yeomans, Modelling capillary filling dynamics using lattice Boltzmann simulations, *Eur Phys J - Special Topics*, 171 (2009) 63-71.
- [51] V. Kocaba, Development and evaluation of methods to follow microstructural development of cementitious systems including slags, Ph.D. thesis, Ecole Polytechnique Fédérale de Lausanne, 2009.
- [52] H.M. Jennings and P.D. Tennis, Model for the Developing Microstructure in Portland Cement Pastes, *J Am Ceram Soc*, 77 (1994) 3161-3172.
- [53] T.C. Powers and T.L. Brownyard, Studies of the physical properties of hardened portland cement paste, Portland Cement Association (Bulletin 22), Chicago (1948), reprinted from *Proc. J. Am. Concr. Inst.* 43 (1947), p. 101, 249, 469, 549, 669, 845, 993.
- [54] H.F.W. Taylor, *Cement chemistry*, Thomas Telford, London, 1997, pp. 238.
- [55] Virtual Cement & Concrete Reference Laboratory database, <http://ciks.cbt.nist.gov/bentz/phpct/database/images>, (accessed 1st December 2011).
- [56] S. Succi, *The lattice Boltzmann equation for fluid dynamics and beyond*, Clarendon Press, Oxford, 2001, pp. 119.
- [57] A.C.A. Muller, K. Scrivener, A. Gajewicz and P.J. McDonald, The density and morphology of calcium-silicate-hydrate in never-dried cement paste measured by bench-top NMR (In preparation).
- [58] Q.H. Do, S. Bishnoi and K. Scrivener, Numerical simulation of porosity in simulated cement systems (Submitted to *Transport Porous Med*, 2012).
- [59] M.A.B. Promentilla, T. Sugiyama, T. Hitomi and N. Takeda, Quantification of tortuosity in hardened cement pastes using synchrotron-based X-ray computed microtomography, *Cem Conc Res*, 39 (2009) 548-557.

- [60] O. Dardis and J. McCloskey, Lattice Boltzmann scheme with real numbered solid density for the simulation of flow in porous media, *Phys Rev E*, 57 (1998) 4834-4837.
- [61] S.D.C. Walsh, H. Burwinkle and M.O. Saar, A new partial-bounceback lattice-Boltzmann method for fluid flow through heterogeneous media, *Computers & Geosciences*, 35 (2009) 1186-1193.
- [62] T.R.R. Pintelon, C. Picioreanu, M.C.M. van Loosdrecht and M.L. Johns, The effect of biofilm permeability on bio-clogging of porous media, *Biotechnology and Bioengineering*, 109 (2012) 1031-1042.
- [63] R.F. Feldman, Helium flow characteristics of rewetted specimens of dried hydrated portland cement paste, *Cem Conc Res*, 3 (1973) 777-790.

Captions, tables and figures

TABLE I. Literature reports of experimentally measured cement intrinsic permeabilities.

TABLE II. Computed permeabilities (10^{-16} m^2) for different microstructure resolutions (1, 0.5 and $0.25 \mu\text{m}$) and lattice magnifications (1, 2 and 4 times). The structure has a water-to-cement ratio of 0.4, a hydration degree of 65% and porosity of 21.5%.

FIG 1. The fractional error in simulated permeability of overlapping spheres as a function of the size of the cubic array of the system. The porosity is held constant at circa 20%.

FIG. 2. (a) The contact angle as a function of surface-normal fluid density gradient for the two-phase model as described in the text, (b) likewise the pressure drop across a liquid drop interface, (c) the capillary rise and (d) pendular rings formed at the contacts between packed spheres. Solid is white, liquid black and gas grey.

FIG. 3. The capillary pore size distributions for a μIC cement sample with $w/c=0.4$ at 0 (squares) and 85% (triangles) degree of hydration. The plot shows the integrated porosity in pores greater than, or equal to, the given radius.

FIG. 4. Calculated permeability as a function of degree of hydration for different water-to-cement ratios: $w/c=0.3$ (squares); $w/c=0.4$ (circles); $w/c=0.5$ (up triangles) and $w/c=0.7$ (down triangles).

FIG. 5. Calculated permeability as a function of porosity for different water-to-cement ratios: $w/c=0.3$ (squares); $w/c=0.4$ (circles); $w/c=0.5$ (up triangles) and $w/c=0.7$ (down triangles).

FIG. 6. Equilibrium phase distribution of fluid in a single cement pore obtained at 3 different reduced temperatures (liquid : vapour density ratios) of (a) 0.95 (2.3 : 1), (b) 0.8 (8.1 : 1) and (c) 0.5 (113 : 1) for a constant bulk liquid volume fraction of $2/3$. Liquid is shown in black, vapour in grey and solid in white.

FIG. 7. The equilibrated distribution of liquid (black) and vapour (grey) in a slice of μC microstructure starting from an initially uniform distribution (see text). Solid is white.

FIG. 8. The simulated capillary desorption and adsorption isotherm for a μC sample. The mass of adsorbed liquid is calculated as the sum of the distribution functions in pores containing liquid. The layer of adsorbed water on the macro-surface of the sample is not included in the calculations. The shaded region shows the variation (standard error in the mean) in the repeated simulations.

FIG. 9. A pair of next-nearest 2D slices at critical vapour pressures during adsorption and desorption of fluid in a μC segment showing the differences in liquid (black) and vapour (grey) distribution. Solid is white. Periodic boundary conditions apply. One pair of opposite surfaces (front-left; back-right) is maintained in contact with the vapour. Starting top-left, the figures going clockwise, are the slices during desorption at 98.3, 96, 87 and 84% RH

followed by the slices during adsorption at 84, 87, 96 and 98.3% RH. The two bulk surface adsorbed liquid layers are seen at 98.3% RH (desorption); one remains at 96% RH.

TABLE I

	Method	w/c	Hydration age (days)	Intrinsic permeability (m²)
T.C. Powers <i>et al.</i> (1955) [5]	Pressure-induced (water)	0.7	Fresh to 28	2×10^{-13} to 6×10^{-19}
B.K. Nyame and J.M. Illston (1981) [6]	Pressure-induced (water)	0.23	3 to 600	10^{-19} to 2×10^{-22}
		0.47		5.1×10^{-17} to 3.1×10^{-22}
		0.71		2×10^{-15} to 10^{-20}
N. Banthia and S. Mindess (1989) [7]	Pressure-induced (water)	0.35	1 to 28	2.5×10^{-17} to 6.4×10^{-20}
W. Vichit-Vadakan and G.W. Scherer (2004) [8]	Beam bending (water)	0.4	3 to 14	4×10^{-21} to 3×10^{-22}
		0.5	3 to 21	2×10^{-20} to 10^{-21}
		0.6	5 to 14	10^{-19} to 6×10^{-21}
G. Ye (2005) [9]	Pressure-induced (water)	0.4	3 to 28	6.6×10^{-19} to 9.2×10^{-21}
		0.5		1.6×10^{-17} to 1.4×10^{-19}
		0.6		4.7×10^{-17} to 1.9×10^{-18}
Z.C. Grasley and G.W. Scherer (2007) [10]	Dynamic pressurization (water)	0.4	5 to 14	5×10^{-21} to 10^{-21}
		0.5	3 to 32	10^{-19} to 10^{-21}
		0.6	32	7×10^{-21}
Wong <i>et al.</i> (2009) [11]	Pressure-induced (oxygen)	0.3	90	4×10^{-17}
		0.45		6.5×10^{-17}

TABLE II

		Lattice magnification		
		1	2	4
Microstructure resolution (μm)	1	28.5	10.8	2.66
	0.5	14.7	5.48	
	0.25	7.43		

Fig. 1

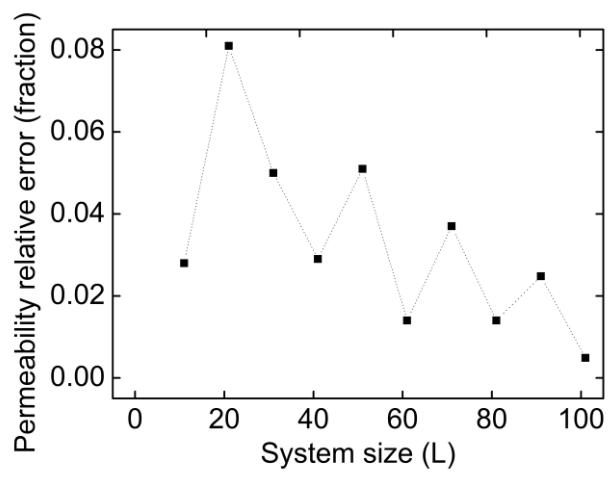


Fig. 2

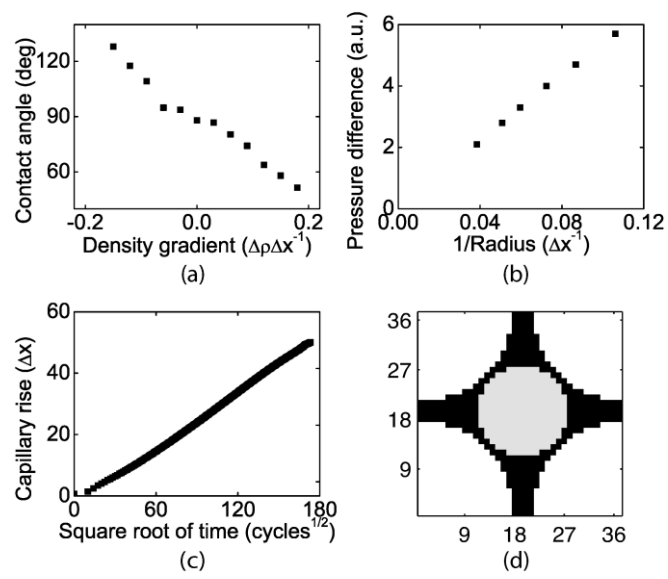


Fig. 3

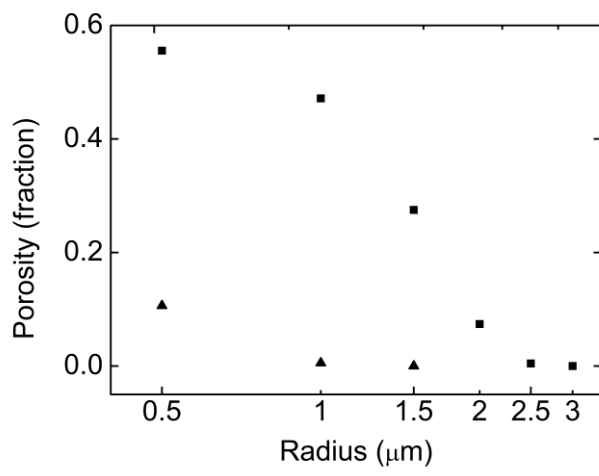


Fig. 4

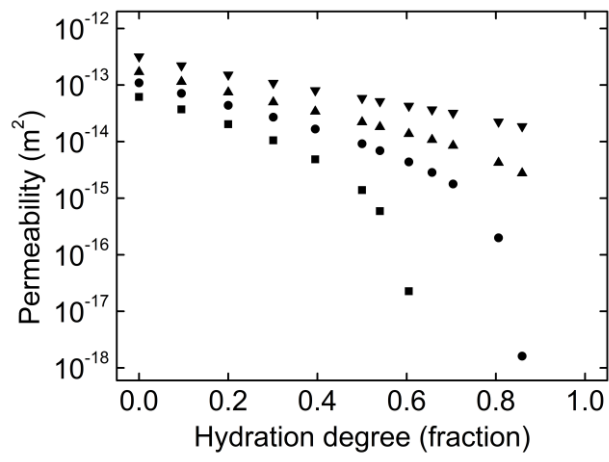


Fig. 5

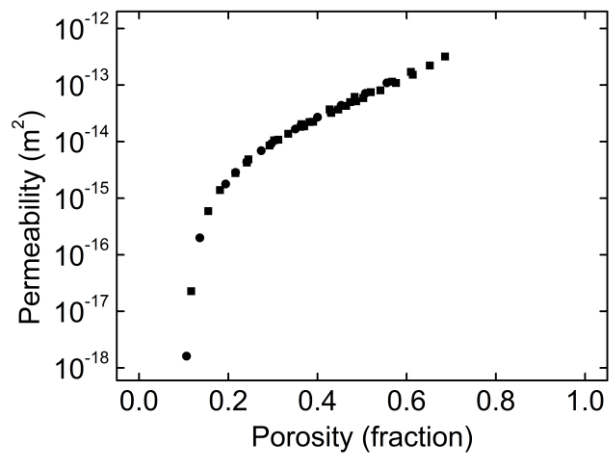


Fig. 6

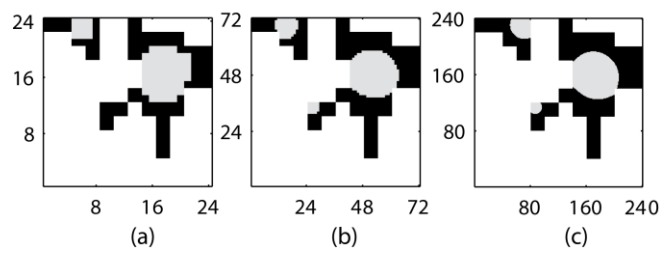


Fig. 7

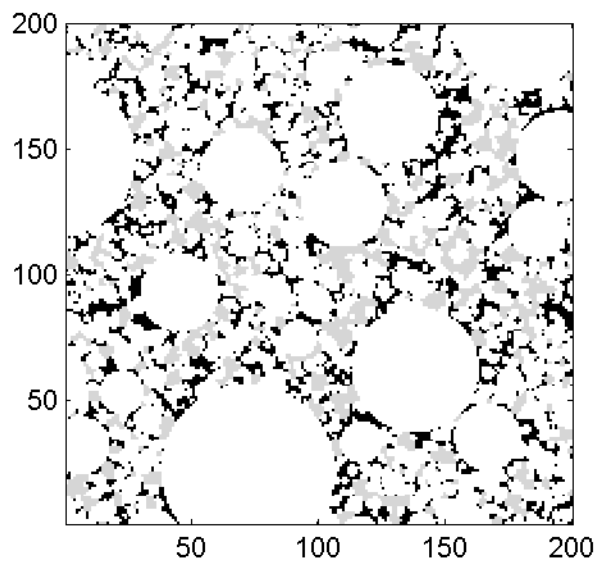


Fig. 8

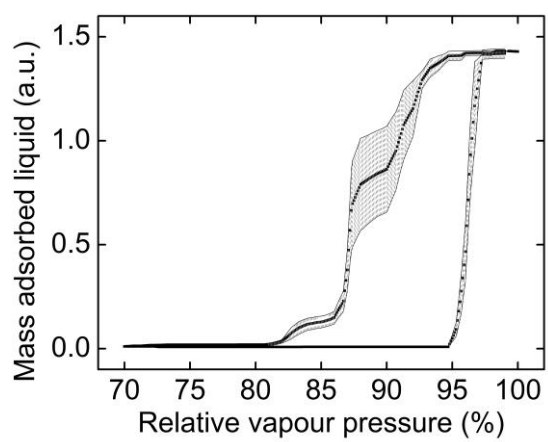


Fig. 9

